Mathematical Biosciences and Engineering

MBE, 18(5): 5978–5994.
DOI: 10.3934/mbe.2021299
Received: 15 April 2021
Accepted: 23 June 2021
Published: 02 July 2021

http://www.aimspress.com/journal/MBE

Research article

Branch flow distribution approach and its application in the calculation of fractional flow reserve in stenotic coronary artery

Honghui Zhang[1,2], Jun Xia[1,2], Yinlong Yang[1,2], Qingqing Yang[1,2], Hongfang Song[3], Jinjie Xie[4], Yue Ma[5], Yang Hou[5] and Aike Qiao[1,2,*]

[1] Faculty of Environment and Life, Beijing University of Technology, Beijing 100124, China
[2] Intelligent Physiological Measurement and Clinical Translation, Beijing International Base for Scientific and Technological Cooperation, Beijing 100124, China
[3] School of Biomedical Engineering, Beijing Key Laboratory of Fundamental Research on Biomechanics in Clinical Application, Capital Medical University, Beijing 100069, China
[4] Beijing Anzhen Hospital, Capital Medical University, Beijing 100029, China
[5] Shengjing Hospital, China Medical University, Shenyang 110001, China

* **Correspondence:** Email: qak@bjut.edu.cn; Tel: +861067396657; Fax: +861067396657.

Abstract: *Objective:* To calculate fractional flow reserve (FFR) based on computed tomography angiography (i.e., FFR_{CT}) by considering the branch flow distribution in the coronary arteries. *Background:* FFR is the gold standard to diagnose myocardial ischemia caused by coronary stenosis. An accurate and noninvasive method for obtaining total coronary blood flow is needed for the calculation of FFR_{CT}. *Methods:* A mathematical model for estimating the coronary blood flow rate and two approaches for setting the patient-specific flow boundary condition were proposed. Coronary branch flow distribution methods based on a volume-flow approach and a diameter-flow approach were employed for the numerical simulation of FFR_{CT}. The values of simulated FFR_{CT} for 16 patients were compared with their clinically measured FFR. *Results:* The ratio of total coronary blood flow to cardiac output and the myocardial blood flow under the condition of hyperemia were 16.97% and 4.07 mL/min/g, respectively. The errors of FFR_{CT} compared with clinical data under the volume-flow approach and diameter-flow approach were 10.47% and 11.76%, respectively, the diagnostic accuracies of FFR_{CT} were 65% and 85%, and the consistencies were 95% and 90%. *Conclusions:* The mathematical model for estimating the coronary blood flow rate and the coronary branch flow distribution method can be applied to calculate the value of clinical noninvasive FFR_{CT}.

Keywords: coronary artery disease; hemodynamics; endovascular intervention; catheterization; diagnosis

1. Introduction

Coronary artery disease (CAD) develops when coronary arteries become damaged or diseased because of the dominant prevalence of stenosis. Relying only on anatomical information when doing noninvasive or invasive coronary angiography has proven to be insufficient to detect hemodynamically significant epicardial stenosis [1]. Invasive fractional flow reserve (FFR) has been accepted as the gold standard because of its high accuracy for the assessment of myocardial ischemia [2]. FFR determines the likelihood that the stenosis is impeding oxygen delivery to the heart muscle, and it is defined as the pressure after (distal to) a stenosis relative to the pressure before (proximal to) the stenosis. However, the application rate of gold standard invasive FFR in clinical practice is low, mainly due to its high measurement cost and potential risks during catheter insertion [3].

Clinical vascular stenosis measurement by invasive FFR [4] can be effectively solved by calculating computed tomography (CT) angiography-derived noninvasive fractional flow reserve (FFR_{CT}) with the help of computational fluid dynamics (CFD) solvers [5–7]. Noninvasive FFR_{CT} provides incremental diagnostic value over coronary CT angiography (CCTA) alone by adding functional information [8]. Over the past decade, a series of randomized trials have established noninvasive CCTA as a safe and potentially cost-effective strategy in the workup of patients with acute chest pain and low-intermediate risk of acute coronary syndrome who present to the emergency department [9].

FFR_{CT} has been widely used and studied by clinicians and researchers in recent years. The diagnostic performance of FFR_{CT} has been investigated experimentally by some multicenter studies, including DISCOVER-FLOW (Diagnosis of Ischemia-Causing Stenoses Obtained Via Noninvasive Fractional Flow Reserve) [10,11], DeFACTO (Determination of Fractional Flow Reserve by Anatomic Computed Tomographic Angiography) [12–15] and NXT (Analysis of Coronary Blood Flow Using CT Angiography: Next Steps) [16–19], comprising a total of 609 patients and 1050 vessels. The trial in 2014 showed that the accuracy of FFR_{CT} was 81% [17], which needs to be improved to satisfy clinical requirements. Recently, a total of 338 consecutive patients with 422 vessels from 9 Chinese medical centers undergoing CCTA and invasive FFR were retrospectively analyzed. Their FFR_{CT} values were obtained as a novel on-site computational fluid dynamics-based FFR_{CT} (uCT-FFR). A new model of FFR_{CT} relying on boundary conditions derived from structural deformation of the coronary lumen and aorta, with a transluminal attenuation gradient and assumptions regarding microvascular resistance, was developed and applied to assess the performance characteristics of uCT-FFR and CCTA in detecting lesion-specific ischemia in all lesions, intermediate lesions (luminal stenosis 30 to 70%), and "gray zone" lesions (FFR 0.75 to 0.80). The accuracy of this novel approach reached 91% [20]. A prospective, multicenter, cross-sectional study, Dan-NICAD 2, including approximately 2000 patients with low to intermediate pretest probability of CAD and without previous history of CAD, is an ongoing study [21] that is expected to contribute to the improvement of diagnostic strategies for patients suspected of CAD in 3 different steps: risk stratification prior to coronary CTA, diagnostic strategy after coronary CTA, and invasive wireless quantitative flow ratio (QFR) analysis as an alternative to invasive FFR.

The insufficient accuracy of FFR_{CT} is the major obstacle to progress in its clinical application. The main aspects of modeling that affect FFR_{CT} estimation are the accuracy of the model reconstruction, the choice of inlet and outlet boundary conditions and the estimation of the flow distribution in the coronary network [22], where the boundary condition directly determines the blood flow pattern. Boundary condition settings can be simplified by calculating the total coronary blood flow [5]. The calculation of total coronary blood flow could be completed based on the scaling relationship between myocardial mass and coronary blood flow [23]. However, myocardial mass is not the only factor affecting coronary blood flow, and there are individual differences in the correlation between myocardial mass and total coronary blood flow. Heart rate and aortic peak systolic pressure were input into the mathematical model of coronary blood flow of Arthurs et al [24]. This model can provide patient-specific estimates of coronary blood flow changes between rest and exercise situations. Duanmu et al. considered the ventricular contraction function of patients and simulated patient-specific coronary blood flow changes under intramyocardial stress changes at the terminus of the coronary artery [25]. Duanmu et al. incorporated the head loss at the junctions of inlets to could provide patient-specific estimates of coronary blood flow changes under cross-sectional area changes at the inlets of the coronary arteries [26]. In addition to heart rate and aortic peak systole pressure, ventricular contraction function and head loss at the junctions of inlets were also considered input parameters, but they were not easy to detect.

In the studies of Taylor et al and Choy et al. [5,23], the myocardial mass satisfied the power law, the diameter and length of branch arteries having exponents of 3/8 and 3/4, respectively. Huo et al established the scaling law on length and volume relationship with an exponent of 7/9 based on experiments with rats of different ages [27]. These mathematical models provide approaches to calculate the distribution of flow rates in coronary artery branches. However, the models by Choy 2008 and Huo 2009 are based on animal experimental data, so they might not be applicable to human beings.

Based on this situation, this study proposed a FFR_{CT} calculation method with personalized boundary conditions, which can realize the non-invasive simulation of coronary blood flow distribution and assist the clinical treatment of coronary stenosis.

2. Methods

2.1. Geometry model of coronary artery

The exclusion criteria for this study were as follows: 1) myocardial damage or recent myocardial infarction (within one month); 2) left ventricular dysfunction; 3) significant 3-vessel disease; and 4) poor-quality CT images. All patients underwent CCTA and coronary FFR. Intravenous adenosine (140 μg/kg/min) was administered to the inlet coronary artery to induce maximum hyperemia. Based on the maximum hyperemia value, we obtained the pressure waveform of the aortic pressure (P_a) and distal arterial pressure (P_d) using a pressure guide wire. We further calculated FFR as the ratio of the mean pressure at a cross-section 3 cm downstream of the stenosis (P_d) to the mean pressure at the coronary entry region (P_a) during maximal hyperemia [5,28]. Sixteen patients with steady coronary artery disease were included in our study. Among them, 20 vessels with coronary stenosis were included, 14 (88%) with right coronary artery dominance. Informed consent was waived due to the retrospective nature of the study.

Medical image segmentation and 3D reconstruction of the geometric model of coronary and aortic roots were accomplished by using the commercial tool MIMICS (Materialise, Leuven, Belgium). Vessels with diameters larger than 1 mm were saved and reconstructed. The centerline of each vessel was identified, and the diameter of each vessel was calculated by manually selecting each vessel in MIMICS. Then, the tool Freeform (Artec 3d, Luxembourg) was used to remove the noise in the 3D model, and the software GEOMAGIC (Geomagic, Research Triangle Park, North Carolina) was used to repair and further optimize the model surface. GEOMAGIC software was used to further optimize the model surface and calculate the volume of the 3D model. Then, a branch of the coronary artery was cut in the 3D model, and the volume of the remaining 3D model was calculated using GEOMAGIC. The volume of a branch of the coronary artery was the volume change before and after cutting the 3D model. Repeating the above operation on each vessel of the 3D model, the volume of each vessel of the coronary artery was calculated for further research. SOLIDWORKS (Dassault Systemes, Waltham, Massachusetts) was used to cut the entrance port into a plat section. Finally, the geometric model was imported to ANASYS CFX (ANSYS Corporation, Canonsburg, Pennsylvania) for hemodynamics simulation.

2.2. Mathematic model of coronary blood flow rate

Myocardium is perfused by coronary arteries. Some coronary vessels buried deeply in the myocardium will be compressed during cardiac systole, which will affect coronary blood flow. Blood flow will reach a climax at early diastole and then decelerate slowly [29]. In general, coronary blood flow during left ventricular systole is only 20–30% of that during diastole and will decrease when myocardial contraction strengthens.

Some independent physiological parameters, including myocardial mass, diastolic blood pressure and heart rate, were selected to calculate coronary blood flow.

Myocardial mass. The scaling laws between coronary blood flow (Q_{cor}) and the myocardial mass (M) can be described by Eq (1) [23]:

$$Q_{cor} \propto M^{0.75} \tag{1}$$

In a broad sense, the myocardium includes the right ventricular myocardium, atrial myocardium and other myocardial tissue in addition to the left ventricular myocardium. The left ventricular myocardial mass (M_L) accounts for approximately 85% of the total myocardial mass [30,31]. Therefore, the scaling law can be revised as Eq (2):

$$Q_{cor} \propto (M_L/0.85)^{0.75} \tag{2}$$

Diastolic blood pressure. Coronary perfusion is mainly affected by diastolic blood pressure since coronary blood flow perfusion is mainly accomplished in diastole. According to Poiseuille's law, Eq (3) is satisfied:

$$Q_{cor} = \Delta P(\pi r^4/8\eta L) \tag{3}$$

where the perfusion pressure $\triangle P$, which is the pressure drop along the artery with a length of L, can be calculated from Eq (4),

$$\Delta P = P_D - P_{Ra} \tag{4}$$

where P_D is the aortic diastolic blood pressure and P_{Ra} is the right atrial pressure (-2–10 mmHg). Studies have shown that aortic diastolic blood pressure can be used alone to calculate the coronary blood flow rate, and diastolic blood pressure is proportional to the coronary blood flow rate [32–34]. For the sake of simplification, the perfusion pressure was set as the aortic diastolic blood pressure by ignoring the right atrial pressure in this study. This let the relationship between coronary blood flow rate and diastolic blood pressure be described by Eq (5):

$$Q_{cor} \propto P_D \tag{5}$$

Heart rate. Effective perfusion time is another factor affecting coronary blood flow. The diastole of a cardiac cycle is the time for coronary blood perfusion [29]. Diastolic duration (*T*) becomes relatively compressed with increasing heart rate (*HR*).

According to the correlation between heart rate and diastolic duration (Figure 1) [35], the perfusion time per minute can be described as a function of heart rate as in Eq (6):

$$T_m = T * HR = HR[-0.568\ln(HR) + 3.246] \tag{6}$$

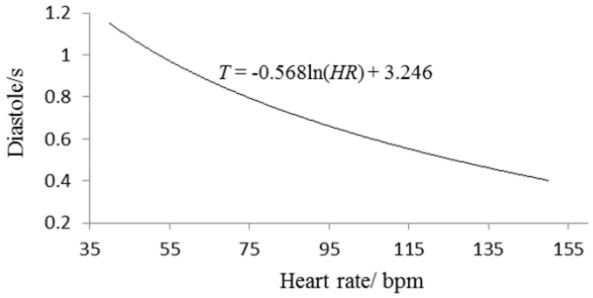

Figure 1. Correlation between left ventricular diastole and heart rate during a cardiac cycle.

As the perfusion rate is assumed to be constant, the blood flow of the coronary artery is proportional to the perfusion time. Then, the relationship between coronary blood flow rate and heart rate can be described by Eq (7):

$$Q_{cor} \propto HR[-0.568\ln(HR) + 3.246] \tag{7}$$

Combining Eqs (2), (5) and (7), the mathematical model of coronary blood flow rate during maximal hyperemia with adenosine can be established as Eq (8):

$$Q_{cor} = kHR[-0.568\ln(HR) + 3.246]P_D(M_L/0.85)^{0.75} \tag{8}$$

where *k* is a constant coefficient that needs to be determined according to clinical data.

Due to the lack of clinical data, coronary blood flow was derived from the simulation in this study. Twenty-nine randomly selected patients with mild stenosis and FFR < 0.90 were adopted to perform the simulation and calculate the value of *k* that made the simulation result close to the real physiological value. The value of *k* for this study was the average of those from the 29 patients.

FFR_{CT} was the ratio of the mean pressure at a cross-section 3 cm downstream of the stenosis (P_d) to the mean pressure at the coronary entry region (P_a) [5]. Figure 2 shows the technical flow of coronary FFR_{CT}. First, a three-dimensional model of the coronary artery was reconstructed from CCTA. Blood was modeled as a Newtonian fluid, and the blood density and dynamic viscosity were constants with

values of 1050 kg/m^3 and 0.0035 Pa·s, respectively [28]. The blood flow was steady, and the material properties of the arterial walls were rigid.

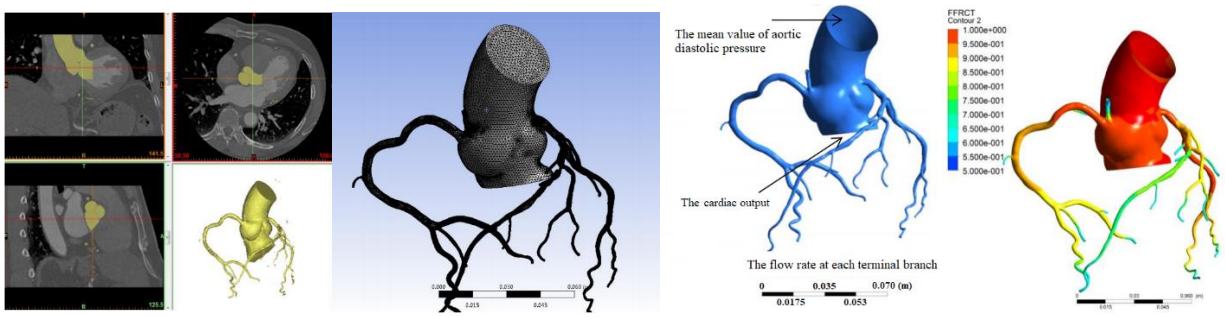

(a) (b) (c) (d)

Figure 2. Technical flow chart of calculating coronary FFR_{CT}. (a) 3D reconstruction of the coronary artery model based on CCTA; (b) meshing of fluid and boundary layer; (c) individualized settings of the boundary conditions; (d) CFD simulation calculation and postprocessing

The mesh of the geometries was generated by using nonstructural tetrahedron elements. To improve the accuracy of the boundary layer calculation, the boundary layer near the vessel wall was set to three layers. After testing the target residual and convergence step dependence, the target residual was determined to be 1e-4. The cardiac output at the root of the aorta was assigned as the inlet boundary condition. The mean value of aortic diastolic pressure at the outlet of the aorta was assigned as the outlet boundary condition. Based on the mean value of the coronary blood flow rate of the patient, the coronary blood flow rate was initialized as the product of myocardial mass and myocardial blood flow during hyperemia, at 3.37 mL/min/g [36]. The blood flow rate in a vessel was proportional to the 3rd power of the vessel diameter according to Poiseuille's solution and Murray's law [37]. The flow rate at each terminal branch was identified as the outlet boundary condition. Simulations were carried out by using ANSYS Workbench. Steady flow simulation was employed to significantly reduce the computational cost. The computational time of FFR_{CT} was only 10 minutes, which was 24-fold less than with Taylor's method [5].

The coronary blood flow rate was initialized as the product of myocardial mass and myocardial blood flow during hyperemia, at 3.37 mL/min/g [36], which is the mean value in humans, and then it was updated according to the following steps until the simulation result of FFR_{CT} matched the invasive FFR value.

(a) Perform simulation with the initial value of flow rate, and calculate the coronary FFR_{CT} from the simulation results.

(b) If the simulation result of FFR_{CT} was larger than the invasive value of FFR, increase the coronary blood flow rate; otherwise, decrease it.

(c) Adjust the flow rate by 50, 20, 10, and 5 mL/min until the simulation result of FFR_{CT} matched the invasive value of FFR.

(d) Take the matched flow rate as the reference coronary blood flow rate.

(e) Substitute the reference coronary blood flow rate into Eq (6) to solve for the constant *k*. The mean value of *k* (*k=0.003*) obtained from the 29 patients was taken as the value of *k* in the mathematical model, and thus Eq (8) could be written as Eq (9):

$$Q_{cor} = 0.003HR[-0.568\ln(HR) + 3.246]P_D(M_L/0.85)^{0.75} \quad (9)$$

Then, Eq (9) was applied to perform the simulation for the 20 vessels with coronary stenosis in our 16 patients.

2.3. Branch flow distribution approaches for coronary artery

Several morphological (diameter, length, and volume) and functional (flow) parameters of the coronary arterial tree related to myocardial mass were quantified in in vitro animal experiments by Choy et al [23]. The results showed that arterial volume was linearly related to regional myocardial mass [23], whereas the sum of coronary arterial branch lengths, vessel diameters, and volumetric flow showed a 3/4, 3/8, and 3/4 power-law relationship, respectively. These findings were consistent with the earlier experimental results of Seiler et al [38,39]. Based on the physiological observation that longer coronary arteries have more daughter branches feeding a larger mass of cardiac muscle, Lee et al presented a vessel length-based method calculating the coronary flow distribution over coronary major arteries [40].

Given that the volume of a vessel contains its diameter and the length, we proposed a vessel volume-based method to calculate the flow distribution over coronary major arteries. Since the arterial volume is linearly related to regional myocardial mass [23], the regional myocardial mass of the left anterior descending (LAD) artery, the left circumflex (LCX) artery, and the right coronary artery (RCA) can be described by Eq (10):

$$M_{LAD} = \alpha V_{vessel-LAD};\ M_{LCX} = \alpha V_{vessel-LCX};\ M_{RCA} = \alpha V_{vessel-RCA} \quad (10)$$

where M_{LAD}, M_{LCX} and M_{RCA} represent the regional myocardial mass of the LAD, LCX and RCA, respectively; $V_{vessel\text{-}LAD}$, $V_{vessel\text{-}LCX}$ and $V_{vessel\text{-}RCA}$ represent the vessel volume of the LAD, LCX and RCA, respectively; and α is a constant scale coefficient.

The volumetric flow shows a 0.75 power-law relationship with myocardial mass, so Eq (11) can be obtained:

$$Q_{LAD} = \beta {M_{LAD}}^{0.75};\ Q_{LCX} = \beta {M_{LCX}}^{0.75};\ Q_{RCA} = \beta {M_{RCA}}^{0.75} \quad (11)$$

where Q_{LAD}, Q_{LCX} and Q_{RCA} represent the volumetric flow of the LAD, LCX and RCA respectively, and β is a constant scale coefficient.

Equation (12) can be deduced from the above two equations. Namely, the volumetric flow shows a 0.75 power-law relationship with the vessel volume. Although such a relationship was not presented in the paper by Choy 2008 [23], it follows from the results presented therein, but it has had no direct experimental validation:

$$Q_{LAD} = \alpha^{0.75}\beta {V_{vessel-LAD}}^{0.75};\ Q_{LCX} = \alpha^{0.75}\beta {V_{vessel-LCX}}^{0.75};\ Q_{RCA} = \alpha^{0.75}\beta {V_{vessel-RCA}}^{0.75} \quad (12)$$

The total coronary blood flow rate is the sum of the blood flow rate over the LAD, LCX and RCA, as shown in Eq (13):

$$Q_{cor} = Q_{LAD} + Q_{LCX} + Q_{RCA} \quad (13)$$

The flow distributions of the LAD, LCX and RCA is respectively are described in Eq (14):

$$\begin{aligned} Q_{LAD} &= Q_{cor}[{V_{vessel-LAD}}^{0.75}/({V_{vessel-LAD}}^{0.75} + {V_{vessel-LCX}}^{0.75} + {V_{vessel-RCA}}^{0.75})] \\ Q_{LCX} &= Q_{cor}[{V_{vessel-LCX}}^{0.75}/({V_{vessel-LAD}}^{0.75} + {V_{vessel-LCX}}^{0.75} + {V_{vessel-RCA}}^{0.75})] \\ Q_{RCA} &= Q_{cor}[{V_{vessel-RCA}}^{0.75}/({V_{vessel-LAD}}^{0.75} + {V_{vessel-LCX}}^{0.75} + {V_{vessel-RCA}}^{0.75})] \end{aligned} \quad (14)$$

Ideally, the blood flow rate in a vessel is proportional to the 3rd power of the vessel diameter according to Poiseuille's solution and Murray's law [36], as in Eq (15):

$$Q = (\pi d^3/4)\sqrt{\lambda/\mu} \quad (15)$$

where Q is the flow rate through a blood vessel, d is its diameter, μ is the fluid viscosity, and λ is a constant. This equation represents the energy consumed by the metabolism per unit volume.

If d_{LAD}, d_{LCX}, and d_{RCA} are respectively assigned as the ostium diameter of each branch of the LAD, LCX and RCA (the ostium diameter of each branch can be estimated according to the cross-sectional area of the branch), the flow rate of each branch can be inferred from Eqs (15) and (16) can be obtained:

$$\begin{aligned} Q_{LAD-j} &= Q_{LAD}\left({d_{LAD-j}}^3/\textstyle\sum_{i=1}^{n} {d_{LAD-i}}^3\right) \\ Q_{LCX-j} &= Q_{LCX}\left({d_{LCX-j}}^3/\textstyle\sum_{i=1}^{m} {d_{LCX-i}}^3\right) \\ Q_{RCA-j} &= Q_{RCA}\left({d_{RCA-j}}^3/\textstyle\sum_{i=1}^{s} {d_{RCA-i}}^3\right) \end{aligned} \quad (16)$$

where i and j are, respectively, the number of terminals and the identity of any branch of the LAD, LCX or RCA; and n, m and s are the total number of terminal branches of the LAD, LCX and RCA, respectively.

The coronary artery model reconstructed from CCTA does not completely satisfy Murray's law, so Eq (16) needs to be modified as follows. The flow distribution of each branch was calculated in the direction of blood flow according to the classification of vascular branches, as shown in Figure 3, where di and dij ($i, j = 1, 2$) represent the diameter of each daughter branch of the coronary artery, and Rij ($i, j = 1, 2$) represents the ratio of the flow rate at branch ij to that at the major root. This flow distribution approach was defined as the diameter-flow approach. The diameter-flow relationship showed that the blood flow rate in a vessel was proportional to the 3rd power of the vessel diameter.

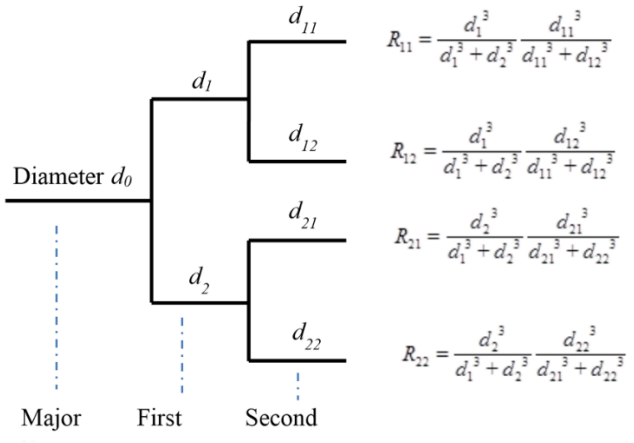

Figure 3. Schematic diagram of the diversion ratio calculation (R represents the diversion ratio).

Similarly, we can assume that the flow rate is proportional to the volume of the corresponding coronary branches: $Q \propto V$. As shown in Figure 4, $Q_0=Q_1+Q_2$; $Q_1=Q_{11}+Q_{12}$; $Q_2=Q_{21}+Q_{22}$; $Q_1:Q_2=V_1^{0.75}:V_2^{0.75}$; $Q_{11}:Q_{12}=V_{11}^{0.75}:V_{12}^{0.75}$; $Q_{21}:Q_{22}=V_{21}^{0.75}:V_{22}^{0.75}$ ... This flow distribution approach was defined as the volume-flow approach. The volume-flow relationship showed that the blood flow rate in a vessel was proportional to the 0.75 power of the vessel volume.

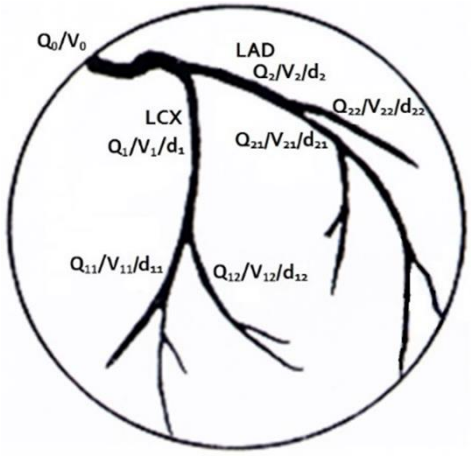

Figure 4. Diagram of flow distribution in branch vessels.

Based on the mean values of aortic diastolic pressure, myocardial mass and heart rate of the patient, we calculated a patient-specific coronary blood flow rate. Based on the volume or diameter from CCTA, we achieved patient-specific distribution of the blood flow rate. Based on the coronary blood flow rate and the distribution rule, we achieved a patient-specific coronary blood flow rate at each terminal branch. Combining the mean value of aortic diastolic pressure as the inlet boundary condition and the coronary blood flow rate at each terminal branch as the outlet boundary condition, we obtained the patient-specific boundary conditions of the fluid dynamics analysis.

2.4. Application of the calculation of FFR_{CT} of coronary stenosis

Based on the two approaches to the patient-specific boundary conditions of the fluid dynamics analysis, the distribution of pressure in a vessel was identified to calculate the FFR_{CT} value.

As measures of the performance of the two approaches in calculating FFR_{CT}, we chose the relative error and the diagnostic accuracy at the threshold of FFR $\leq$ 0.80 through comparison with the clinical FFR values of all 20 vessels with coronary stenosis of the 16 patients. To evaluate the consistency of the two approaches with the clinically measured FFR, we used the consistency with the 95% CI of the Bland-Altman method and the metrics of sensitivity, specificity, positive predictive value (PPV) and negative predictive value (NPV).

3. Results

Based on the information of 29 patients, including the mean values of aortic diastolic pressure, myocardial mass and heart rate, we obtained a mean value of k of 0.003. The distribution of the parameters is shown in Table 1.

Table 1. The distribution of the parameters to identify the coronary blood flow rate.

Parameter details	Range
The mean value of aortic diastolic pressure	51–101 mmHg
Myocardial mass	98–186 g
Heart rate	57–96 bpm
Cardiac output	2.75–6.9 L/min
The coronary blood flow rate	2.3–5.19 ml/min

Based on the structure of the coronary artery from CCTA, we used the diameter-flow approach and volume-flow approach to calculate the corresponding FFR_{CT} values. The distribution of the parameters of the two approaches is shown in Table 2, and they were within the range of numbers in previous coronary morphology studies [23,28]. Based on Eqs (10) and (11), the regional myocardial masses of the LAD, LCX and RCA were replaced by the corresponding blood vessel volumes. The blood vessel volumes of the LAD, LCX and RCA are shown in Table 2.

Table 2. The distribution of the parameters of 16 patients.

Parameter details	Range
The mean value of aortic diastolic pressure	70–98 mmHg
Myocardial mass	96–175 g
Heart rate	54–84 bpm
Cardiac output	2.1–6.3 L/min
$V_{vessel\text{-}LAD}$	502.46–2755.81 mm^3
$V_{vessel\text{-}LCX}$	432.42–1855.67 mm^3
$V_{vessel\text{-}RCA}$	316.6–924.18 mm^3
d_1	3.12–3.88 mm
d_{11}	2.78–2.89 mm
d_{12}	2.64–2.96 mm
d_2	2.11–2.44 mm
d_{21}	1.13–1.88 mm
d_{22}	1.02–1.66 mm
V_1	76.42–118.82 mm^3
V_{11}	151.7–163.9 mm^3
V_{12}	158.7–199.5 mm^3
V_2	139.79–186.94 mm^3
V_{21}	60.14–166.47 mm^3
V_{22}	57.17–151.42 mm^3

3.1. Rationality

Due to the lack of actual values of clinical coronary blood flow, the ratio of total coronary blood flow to cardiac output (Per_Q) and myocardial blood flow (Q_{myo}) were selected as the evaluation indices to assess the rationality of the model of coronary blood flow. The mean values of Per_Q and Q_{myo} in the 20 vessels with coronary stenosis of the 16 patients, under the condition of hyperemia, were 16.97% and 4.07 mL/min/g, respectively, which were in accordance with the rule of medical statistics [36].

The coronary flow distribution to coronary major branches for 20 vessels with coronary stenosis was calculated (Table 3), and they were almost identical to those based on clinical measurements [41].

Table 3. Average fraction of coronary flow distribution for LAD, LCX, and RCA.

	LAD (%)	LCX (%)	RCA (%)
Calculated data	32.9	20.6	46.5
Clinical data (Sakamoto 2013)	31.1	26.7	41.9

3.2. Accuracy

The diagnostic performance of FFR_{CT} was estimated by the reference of clinical coronary FFR, with $FFR \leq 0.80$ as the threshold. The relative errors between the FFR_{CT} based on CFD simulation and the invasively measured FFR were obtained. These relative errors were 10.47% and 11.76%, respectively, under the volume-flow relationship and diameter-flow relationship. These differences may have arisen both from the neglect of branches with diameters less than 1 mm and from the subjective operation of the 3D model reconstruction and smoothing. Table 4 shows the results of P_a and P_d and the flow rates of the diameter-flow and volume-flow approaches.

Table 4. The pressure and flow rates of different vessels.

Vessel number	The P_d of diameter approach (mmHg)	The P_d of volume approach (mmHg)	P_a (mmHg)	The flow rate of diameter approach (ml/min)	The flow rate of volume approach (ml/min)
1	82	83	86	0.158	0.286
2	34	72	85	0.121	0.237
3	56	83	101	0.445	0.704
4	86	79	101	0.305	0.424
5	55	67	70	0.170	0.367
6	84	84	94	0.699	1.06
7	81	76	90	1.284	1.502
8	74	76	82	0.081	0.249
9	74	78	82	0.937	0.949
10	47	49	51	0.062	0.155
11	64	60	92	0.049	0.142
12	90	80	92	0.054	0.126
13	64	67	83	0.125	0.315
14	63	74	80	0.424	0.668
15	67	78	80	0.224	0.375
16	74	69	98	0.343	0.485
17	75	80	85	0.358	0.529
18	83	82	85	0.157	0.252
19	67	72	82	0.293	2.89
20	76	77	87	0.184	0.22

In Table 5, the numbers 2 and 6 represent that 2 vessels were calculated as having $FFR_{CT} \leq 0.8$ and 6 vessels were $FFR_{CT}>0.8$ among the vessels with a clinically measured $FFR \leq 0.8$ in the 20 vessels of the 16 patients. The numbers 1 and 11 indicate that 1 vessel had a calculated $FFR_{CT} \leq 0.8$ and 11 vessels were $FFR_{CT} > 0.8$ among those with a clinically measured $FFR > 0.8$.

Table 5. Diagnostic accuracy of FFF_{CT} based on the volume-flow relationship.

FFR_{CT}	FFR	
	≤ 0.80	＞ 0.80
≤ 0.80	2	1
＞ 0.80	6	11

In Table 6, the numbers 6 and 2 represent that 6 vessels were calculated as having $FFR_{CT} \leq 0.8$ and 2 vessels were $FFR_{CT} > 0.8$ among vessels with a clinically measured $FFR \leq 0.8$ among the 20 vessels. The numbers 1 and 11 indicate that 1 vessel had a calculated $FFR_{CT} \leq 0.8$ and 11 vessels were $FFR_{CT} > 0.8$ among those with a clinically measured $FFR > 0.8$.

Table 6. Diagnostic accuracy of FFF_{CT} based on the diameter-flow relationship.

FFR_{CT}	FFR	
	≤ 0.80	＞ 0.80
≤ 0.80	6	1
＞ 0.80	2	11

The diagnostic accuracies of FFR_{CT} obtained from the volume-flow approach and diameter-flow approach were 65% and 85%, respectively, as illustrated in Tables 5 and 6.

3.3. Consistency

The Bland-Altman method was used to evaluate the consistency of FFR_{CT} and FFR. The 95% confidence interval between FFR_{CT} and FFR was approximately [-0.2, +0.2], and most of the data fell within the interval, which indicated that FFR_{CT} and FFR had good consistency (Figure 5). The consistency was greater than 80%.

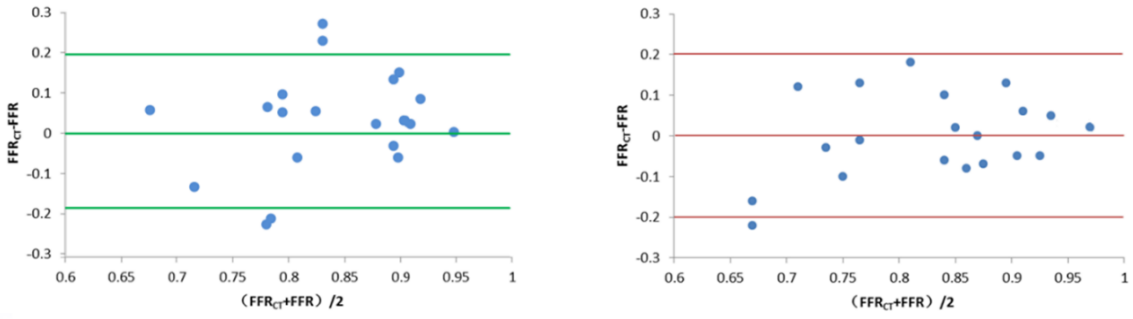

(a) (b)

Figure 5. Bland-Altman diagrams. (a) Volume-flow approach; (b) diameter-flow approach.

The PPV, NPV, sensitivity and specificity under the volume-flow approach were 25%, 91.67%, 66.67% and 64.7%, respectively, and were 75%, 91.67%, 85.71% and 84.62% under the diameter-flow approach.

4. Discussion

This study presented a mathematical model for estimating the coronary blood flow rate and two approaches for setting the patient-specific flow boundary conditions in calculating coronary FFR_{CT}. The present study validated the diagnostic performance of FFR_{CT} compared with invasive FFR.

Under the condition of hyperemia, the flow rate in the coronary artery reaches its peak value, which makes up approximately 15% of the cardiac output [36]. The calculated values of the flow rate in the coronary artery for the 16 patients were similar to the mean values of the human body [36].

With regard to 3D geometric model reconstruction, no more details were investigated in the present study. Because the 3D geometrical model of the coronary arterial tree derived from CT images was used, the spatial resolution in the small-diameter vessels of CCTA could result in deviation between reconstructed geometries and the actual anatomy, adding bias to the stenosis and FFR_{CT} computations [42].

The error of diagnostic accuracy under the volume-flow approach was larger than that under the diameter-flow approach. Compared with clinical FFR, the diagnostic accuracy of noninvasive FFR_{CT}, which is currently widely used in clinics, was 84.3% [10,16,17]. However, this study showed that the diagnostic accuracy of CCTA was only 64%, which meant that CCTA would only be a strategy for preliminary screening of coronary artery stenosis [11–14]. This means CCTA will have difficulty meeting the requirements of clinical use. The large shortcoming may result from the fact that the volume-flow approach is more sensitive to the gray zone of insecurity (with $FFR \leq 0.80$ as the threshold). There is no absolute cutoff point at which the FFR becomes abnormal; rather, there is a smooth transition, with a large gray zone of insecurity. In clinical trials, a cutoff point of 0.75 to 0.80 has been used; higher values indicate nonsignificant stenosis, whereas lower values indicate a significant lesion. Kato et al evaluated the optimal cutoff value of FFR_{CT} by using fluid-structure interactions [43]. They concluded that it was reasonable to support the optimal cutoff value of 0.80 when the disease prevalence is more than 30% if the goal is minimizing 1-year cardiac events. However, underestimation should be adjusted to reduce cardiac events, especially when disease prevalence is low.

There are some limitations to this method. First, individual differences in coronary microcirculation resistance were not considered. Coronary microcirculation resistance, namely, after-loading, which is affected by the activity of the myocardium, directly affects the perfusion of the coronary artery [44]. In this study, we assumed that the patients all had normal coronary microcirculation and had the same response to adenosine and other vasodilator drugs. However, the actual situation is that there is some difference in the coronary microcirculation between different individuals or different regions of individuals, and most of them have different degrees of microcirculatory disturbance [45,46]. Second, the model can only be used in the simulation of coronary arteries during hyperemia. Whether the model can be applied to the resting state still needs to be investigated in depth. Third, the estimated parameter k was based on 29 randomly selected patients. The value of k might change if the set of patients used for estimation has different characteristics. Estimation from a large sample size and precise stratification would be more

representative. Finally, the simulations in this study were all in the steady state, corresponding to the average condition of hyperemia, so the characteristics of pulsatile blood flow were not reflected.

5. Conclusions

A mathematical method to set patient-specific flow boundary conditions was proposed for the sake of exploring the effect of new strategies to specify hyperemic coronary flow and flow distribution parameters in FFR_{CT} simulations. As shown by comparing CCTA assessment, coronary FFR_{CT} and invasive FFR, FFR_{CT} has good consistency with FFR under the proposed patient-specific flow boundary conditions. This study offers a new way to calculate FFR_{CT} and supports the clinical application of FFR_{CT}.

In summary, this work employed coronary blood flow distribution methods based on the volume-flow relationship and diameter-flow relationship to set the boundary conditions in the numerical simulation of FFR_{CT} and compare their application feasibility. The results demonstrated good consistency between the noninvasive value of FFR_{CT} and the invasive value of FFR, even though there were large errors between the diagnostic accuracies of these two methods. The mathematical model for estimating the coronary blood flow rate and the coronary branch flow distribution method can be applied to calculate the value of clinical noninvasive FFR_{CT}. Further in-depth research with large cohorts is needed to modify, verify and clarify the application of the proposed models in the calculation of FFR_{CT}, and an in-depth comparison of the proposed methodology to other methodologies in the literature is needed.

Acknowledgement

This work was supported by National Natural Science Foundation of China (11772015, 11832003).

Conflict of interest

The authors declare that the research was conducted in the absence of any commercial or financial relationships that could be construed as a potential conflict of interest.

References

1. E. Conte, J. Sonck, S. Mushtaq, C. Collet, T. Mizukami, E. Barbato, et al., FFR_{CT} and CT perfusion: A review on the evaluation of functional impact of coronary artery stenosis by cardiac CT, *Int. J. Cardiol.*, **9** (2020), 289–296.
2. A. Cesaro, F. Gragnano, D. D. Girolamo, E. Moscarella, V. Diana, I. Pariggiano, et al., Functional assessment of coronary stenosis: an overview of available techniques. Is quantitative flow ratio a step to the future?, *Expert. Rev. Cardiovasc. Ther.*, **16** (2018), 951–962.
3. G. Y. Li, H. R. Wang, M. Z. Zhang, S. Tupin, A. K. Qiao, Y. J. Liu, et al., Prediction of 3D cardiovascular hemodynamics before and after coronary artery bypass surgery via deep learning, *Commun. Biol.*, **99** (2021), 1–12.
4. N. S. Kleiman, Bringing it all together: integration of physiology with anatomy during cardiac catheterization, *J. Am. Coll. Cardiol.*, **58** (2011), 1219–1221.

5. C. A. Taylor, T. A. Fonte, J. K. Min, Computational fluid dynamics applied to cardiac computed tomography for noninvasive quantification of fractional flow reserve: scientific basis, *J. Am. Coll. Cardiol.*, **61** (2013), 2233–2241.
6. J. K. Min, C. A. Taylor, S. Achenbach, B. K. Koo, J. Leipsic, B. L. Nørgaard, et al., Noninvasive fractional flow reserve derived from coronary CT angiography: clinical data and scientific principles, *JACC Cardiovasc. Imaging*, **8** (2015), 1209–1222.
7. C. Tesche, C. N. D. Cecco, M. H. Albrecht, T. M. Duguay, R. R. Bayer, S. E. Litwin, et al., Coronary CT angiography-derived fractional flow reserve, *Radiology*, **285** (2017), 17–33.
8. M. van Assen, C. N. D. Cecco, M. Eid, P. von Knebel Doeberitz, M. Scarabello, F. Lavra, et al., Prognostic value of CT myocardial perfusion imaging and CT-derived fractional flow reserve for major adverse cardiac events in patients with coronary artery disease, *J. Cardiovasc. Comput. Tomogr.*, **13** (2019), 26–33.
9. K. Nieman. The feasibility, findings and future of CT-FFR in the emergency ward, *J. Cardiovasc. Comput. Tomogr.*, **19** (2019), 287–288.
10. B. K. Koo, A. Erglis, J. H. Doh, D. V. Daniels, S. Jegere, H. S. Kim, et al., Diagnosis of ischemia-causing coronary stenoses by noninvasive fractional flow reserve computed from coronary computed tomographic angiograms. Results from the prospective multicenter DISCOVER-FLOW (diagnosis of ischemia-causing stenoses obtained via noninvasive fractional flow reserve) study, *J. Am. Coll. Cardiol.*, **58** (2011), 1989–1997.
11. J. K. Min, B. K. Koo, A. Erglis, J. H. Doh, D. V. Daniels, S. Jegere, et al., Effect of image quality on diagnostic accuracy of noninvasive fractional flow reserve: results from the prospective multicenter international DISCOVER-FLOW study, *J. Cardiovasc. Comput. Tomogr.*, **6** (2012), 191–199.
12. J. K. Min, D. S. Berman, M. J. Budoff, F. A. Jaffer, J. Leipsic, M. B. Leon MB, et al., Rationale and design of the DeFACTO (determination of fractional flow reserve by anatomic computed tomographic angiography) study, *J. Cardiovasc. Comput. Tomogr.*, **5** (2011), 301–309.
13. J. K. Min, J. Leipsic, M. J. Pencina, D. S. Berman, B. K. Koo, C. van Mieghem, et al., Diagnostic accuracy of fractional flow reserve from anatomic CT angiography, *JAMA*, **308** (2012), 1237–1245.
14. R Nakazato, H. B. Park, D. S. Berman, H. Gransar, B. K. Koo, A. Erglis, et al., Noninvasive fractional flow reserve derived from computed tomography angiography for coronary lesions of intermediate stenosis severity results from the DeFACTO study, *Circ. Cardiovasc. Imaging*, **6** (2013), 881–889.
15. J. Leipsic, T. H. Yang, A. Thompson, B. K. Koo, G. B. J. Mancini, C. Taylor, et al., CT angiography (CTA) and diagnostic performance of noninvasive fractional flow reserve: results from the determination of fractional flow reserve by anatomic CTA (DEFACTO) study, *AJR. Am. J. Roentgenol.*, **202** (2014), 989–994.
16. S. Gaur, S. Achenbach, L. Leipsic, L. Mauri, H. G. Bezerra, Jensen JM, et al., Rationale and design of the HeartFlowNXT (heartflow analysis of coronary blood flow using CT angiography: next steps) study, *J. Cardiovasc. Comput. Tomogr.*, **7**(2013), 279–288.
17. B. L. Nørgaard, J. Leipsic, S. Gaur, S. Seneviratne, B. S. Ko, H. Ito, et al., Diagnostic performance of noninvasive fractional flow reserve derived from coronary computed tomography angiography in suspected coronary artery disease: The NXT trial (analysis of coronary blood flow using CT angiography: next steps), *J. Am. Coll. Cardiol.*, **63** (2014), 1145–1155.

18. T. Miyoshi, K. Osawa, H. Ito, S. Kanazawa, T. Kimura, H, Shiomi, et al., Non-invasive computed fractional flow reserve from computed tomography (CT) for diagnosing coronary artery disease, *Circ. J.*, **79** (2015), 406–412.
19. K. Tanaka, H. G. Bezerra, S. Gaur, G. F. Attizzani, H. E. Bøtker, M. A. Costa, et al., Comparison between nNon-invasive (coronary computed tomography angiography derived) and invasive-fractional flow reserve in patients with serial stenoses within one coronary artery-A NXT trial substudy, *Ann. Biomed. Eng.*, **44** (2016), 580–589.
20. C. X. Tang, C. Y. Liu, M. J. Lu, U. J. Schoepf, C. Tesche, R. R. Bayer, et al., CT FFR for ischemia-specific CAD with a new computational fluid dynamics algorithm: a Chinese multicenter study, *JACC Cardiovasc. Imaging*, **13** (2020), 980–990.
21. L. D. Rasmussen, S. Winther, J. Westra, C. Isaksen, J. A. Ejlersen, L. Brix, et al., Danish study of non-Invasive testing in coronary artery disease 2 (Dan-NICAD 2): Study design for a controlled study of diagnostic accuracy, *Am. Heart. J*, **215** (2019), 114–128.
22. J. M. Carson, S. Pant, C. Roobottom, R. Alcock, Non-invasive coronary CT angiography-derived fractional flow reserve: A benchmark study comparing the diagnostic performance of four different computational methodologies, *Int. J. Numer. Method. Biomed. Eng.*, **17** (2019), e3235.
23. J. S. Choy, G. S. Kassab. Scaling of myocardial mass to flow and morphometry of coronary arteries, *J. Appl. Physiol.*, **104** (2008), 1281–1286.
24. C. J. Arthurs, K. D. Lau, K. N. Asrress, S. R. Redwood, C. A. Figueroa, A mathematical model of coronary blood flow control: simulation of patient-specific three-dimensional hemodynamics during exercise, *Am. J. Physiol. Heart Circ. Physiol.*, **310** (2016), 1242–1258.
25. Z. Duanmu, W. W. Chen, H. Gao, X. L. Yang, X. Luo, N. A. Hill, A one-dimensional hemodynamic model of the coronary arterial tree, *Front. Physiol.*, **10** (2019), 853.
26. Z. Duanmu, M. Yin, X. Fan, X. Yang, X. Luo, A patient-specific lumped-parameter model of coronary circulation, *Sci. Rep.*, **8** (2018), 1–10.
27. Y. Huo, G. S. Kassab, The scaling of blood flow resistance: from a single vessel to the entire distal tree, *Biophys. J.*, **96** (2009), 339–346.
28. J. M. Zhang, L. Zhong, T. Luo, A. M. Lomarda, Y. Huo, J. Yap, et al., Simplified models of non-invasive fractional flow reserve based on CT images, *PLoS One*, **11** (2016), e0153070.
29. M. Abe, H. Tomiyama, H. Yoshida, D. Doba, Diastolic fractional flow reserve to assess the functional severity of moderate coronary artery stenoses: comparison with fractional flow reserve and coronary flow velocity reserve, *Circulation*, **102** (2000), 2365–2370.
30. M. Yang, X. Shen, S. Chen, Assessment of the effect of pulmonary hypertension on right ventricular volume and free wall mass by dynamic three-dimensional voxel imaging of echocardiography, *Chin. J. Uitrasonography*, **7** (2000), 401–404.
31. C. H. Lorenz, E. S. Walker, V. L. Morgan, S. S. Klein, T. P. Graham, Normal human right and left ventricular mass, systolic function, and gender differences by cine magnetic resonance imaging, *J. Cardiovasc. Magn. Res.*, **1** (1999), 7–21.
32. P. Sharma, L. Itu, X. Zheng, A. Kamen, D. Bernhardt, C. Suciu, et al., A framework for personalization of coronary flow computations during rest and hyperemia, *Ann. Int. Conf. IEEE Eng. Med. Biol. Soc.*, 2012, 6665–6668.
33. L. Itu, S. Rapaka, T. Passerini, B. Georgescu, C. Schwemmer, M. Schoebinger, et al., A machine-learning approach for computation of fractional flow reserve from coronary computed tomography, *J. Appl. Physiol.*, **121** (2018), 42–52.

34. H. Anderson, M. Stokes, M. Leon, S. Abu-Halawa, Y. Stuart, R. Kirkeeide, Coronary artery flow velocity is related to lumen area and regional left ventricular mass, *Circulation*, **102** (2000), 48–54.
35. Y. X. Zhao, J. M. Liu, D. G. Xu, X. B. Yan, L. C. Lu, S. Z. Xiao, et al., Population based study of change trend of the ratio of diastolic to systolic duration during exercise, *Chin. J. Appl. Physiol.*, **29** (2013), 134–136.
36. N. G. Uren, J. A. Melin, B. De Brunye, W. Wijns, T. Baudhuin, P. G. Camici, Relation between myocardial blood flow and the severity of coronary-artery stenosis, *N. Engl. J. Med.*, **330** (1994), 1782–1788.
37. C. D. Murray, The physiological principle of minimum work I. the vascular system and the cost of blood volume, *Proc. Natl. Acad. Sci.*, **12** (1926), 207–214.
38. C. Seiler, K. L. Gould, R. L. Kirkeeide, Basic structure-function relations of the epicardial coronary vascular tree. Basis of quantitative coronary arteriography for diffuse coronary artery disease, *Circulation*, **85** (1992), 1987–2003.
39. C. Seiler, R. L. Kirkeeide, K. L. Gould, Measurement from arteriograms of regional myocardial bed size distal to any point in the coronary vascular tree for assessing anatomic area at risk, *J. Am. Coll. Cardiol.*, **21** (1993), 783–797.
40. K. E. Lee, S. S. Kwon, Y. C. Ji, E. S. Shin, J. H. Choi, S. J. Kim, et al., Estimation of the flow resistances exerted in coronary arteries using a vessel length-based method, *Pflugers. Arch.*, **468** (2016), 1–10.
41. S. Sakamoto, S. Takahashi, A. U. Coskun, M. I. Papafaklis, A. Takahashi, S. Saito, et al., Relation of distribution of coronary blood flow volume to coronary artery dominance, *Am. J. Cardiol.*, **111** (2013), 1420–1424.
42. C. A. Bulant, P. J. Blanco, G. D. Maso Talou, C. G. Bezerra, P. A. Lemos, R. A. Feij, A head-to-head comparison between CT- and IVUS-derived coronary blood flow models, *J. Biomech.*, **51** (2017), 65–76.
43. E. Kato, S. Fujimoto, K. K. Kumamaru, Y. O. Kawaguchi, T. Dohi, C. Aoshima, et al., Adjustment of CT-fractional flow reserve based on fluid-structure interaction underestimation to minimize 1-year cardiac events, *Heart Vessels*, **35** (2020), 162–169.
44. H. Mejía-Rentería, J. M. Lee, F. Lauri, N. W. van der Hoeven, G. A de Waard, F. Macaya, et al., Influence of microcirculatory dysfunction on angiography-based functional assessment of coronary stenoses, *JACC Cardiovasc. Interv.*, **23** (2018), 741–753.
45. J. J. Layland, R. J. Whitbourn, A. T. Burns, J. Somaratne, G. Leitl, A. I. Macisaac et al., The index of microvascular resistance identifies patients with periprocedural myocardial infarction in elective percutaneous coronary intervention, *J. Interv. Cardiol.*, **98** (2012), 1492–1497.
46. A. Erkol, S. Pala, C. Kırma, V. Oduncu, C. Dündar, A. Izgi, et al., Relation of circulating osteoprotegerin levels on admission to microvascular obstruction after primary percutaneous coronary intervention, *Am. J. Cardiol.*, **107** (2011), 857–862.

AIMS Press